

***Final Draft***  
**of the original manuscript:**

Li, Y.; Pyczak, F.; Oehring, M.; Wang, L.; Paul, J.; Lorenz, U.; Yao, Z.:

**Thermal stability of Gamma' phase in long-term aged**

**Co-Al-W alloys**

In: Journal of Alloys and Compounds (2017) Elsevier

DOI: [10.1016/j.jallcom.2017.09.157](https://doi.org/10.1016/j.jallcom.2017.09.157)

# Thermal stability of $\gamma'$ phase in long-term aged Co-Al-W alloys

Yuzhi Li<sup>a,\*</sup>, Florian Pyczak<sup>b</sup>, Michael Oehring<sup>b</sup>, Li Wang<sup>b</sup>, Jonathan Paul<sup>b</sup>, Uwe Lorenz<sup>b</sup>, Zekun Yao<sup>a</sup>

a. School of Materials Science and Engineering, Northwestern Polytechnical University, 710072 Xi'an, PR China

b. Institute of Materials Research, Helmholtz-Zentrum Geesthacht, 21502 Geesthacht, Germany

\*Corresponding author. Tel: +862988493744; fax: +862988492642.

E-mail addresses: [liyuzhiyaya@hotmail.com](mailto:liyuzhiyaya@hotmail.com), [liyuzhi@mail.nwpu.edu.cn](mailto:liyuzhi@mail.nwpu.edu.cn) (Yuzhi Li).

**Abstract:** Three cast alloys with compositions of Co-9Al-8W-0.1B, Co-9Al-9W-0.1B and Co-9Al-11W-0.1B (all atomic percent) were aged at 900 °C for 200 h, 500 h, 1000 h, 2000 h, 5000 h and 10000 h to investigate the thermal stability of L1<sub>2</sub> type  $\gamma'$ -Co<sub>3</sub>(Al,W) precipitates. The microstructure during the extended ageing process was observed by Scanning and Transmission Electron Microscopy in order to investigate the evolution of the  $\gamma/\gamma'$  two-phase microstructure and the formation of any additional phases. It was found after 5000 h ageing that four phases,  $\gamma$ ,  $\gamma'$ , D0<sub>19</sub> and B2, were present within the microstructure as identified by X-ray Diffraction combined with Transmission Electron Microscopy and Electron Backscattered Diffraction. The  $\gamma'$  precipitates coarsened according to modified Lifshitz, Slyozov and Wagner theory generally. The fraction of  $\gamma'$  phase decreased while that of D0<sub>19</sub> phase increased contrarily. The phase transformation process from  $\gamma'$ -L1<sub>2</sub> to D0<sub>19</sub> was illustrated by Transmission Electron Microscopy. Stacking faults were identified as the initial step of the decomposition of the  $\gamma'$  phase.

**Keywords:** L1<sub>2</sub>- $\gamma'$  precipitate, thermal stability, precipitates size, volume fraction, stacking faults, L1<sub>2</sub>-D0<sub>19</sub> phase transformation

## 1. Introduction

The discovery of a new type of Co-base superalloys strengthened by a ternary Co<sub>3</sub>(Al,W) compound with an L1<sub>2</sub> ordered structure ( $\gamma'$  phase) was reported by Sato et al. in 2006 [1]. Ni-base superalloys with a similar aligned coherent  $\gamma/\gamma'$  two-phase microstructure are widely known for their excellent high temperature mechanical properties [2]. Prior to the discovery of Sato et al. [1], such hardening effects by  $\gamma'$  phase precipitation were unknown in Co-base superalloys and thus such alloys had a worse high-temperature capability compared to Ni-base superalloys [3]. The discovery of such novel types of Co-base superalloys, which can exhibit a high volume fraction of coherently embedded  $\gamma'$  phase with a solvus up to 1000 °C, offers the possibility of developing similar or even superior mechanical properties compared to the  $\gamma'$  hardened Ni-base superalloys. Taking into account that the melting point of cobalt is

slightly higher than that of nickel, the prospects of attaining better high temperature capability are promising [3-11].

Unfortunately, there is a high degree of uncertainty about the stability of the  $\gamma'$  phase in these novel Co-base superalloys. Some authors report it to be metastable at 1000 °C but stable at 900 °C [1,3-8,12]. However, Kobayashi and Lass et al. [13,14] reported that the  $\gamma'$  precipitates are also metastable at 900 °C and decompose into the hexagonal  $D0_{19}$  phase over time. According to most literature sources [3,9,13-18], no stable  $\gamma/\gamma'$  two-phase region exists in the ternary Co-Al-W system, but the  $\gamma$  matrix phase is in thermodynamic equilibrium with the CoAl (B2) and  $Co_3W$  ( $D0_{19}$ ) phase at 900 °C.

Therefore, to acquire the necessary knowledge to develop this material class into alloys suited for application, it is of high interest to characterize and understand the long-term stability of the  $\gamma/\gamma'$  structure and the mechanisms operating during the transformation of the  $\gamma'$ - $Co_3(Al,W)$  phase into other phases. In order to achieve this, a number of ternary Co-Al-W alloys with W contents between 8 and 11 at.% were heat treated for up to 10000 h and the changes in microstructure, including  $\gamma'$  fraction and particle size, as well as the formation of other phases was investigated. In particular the details of the transformation from  $\gamma'$  phase to  $D0_{19}$  phase during long-term ageing at 900 °C were investigated.

## **2. Experimental procedure**

### *2.1. Sample preparation*

The alloys investigated were Co-9Al-8W-0.1B, Co-9Al-9W-0.1B and Co-9Al-11W-0.1B (all atomic percent in nominal composition), and had been produced by argon arc melting. For the sake of brevity, in the following these alloys will be termed as 8W, 9W and 11W respectively. The ingots were melted from their elements and then remelted 5 times into 64 g buttons to achieve chemical homogeneity. A small amount of boron was added to the alloys to strengthen the grain boundaries and suppress grain boundary fracture. This was done to investigate alloy compositions which could in modified form be suited as polycrystalline material for industrial applications [19] and to ensure that the polycrystalline specimens were suited for mechanical testing without premature failure at grain boundaries [20]. For comparison purposes by the same method a boron free specimen with the composition Co-9Al-9W was also produced.

### *2.2. Heat-treatment*

Solution heat-treatment was conducted at 1300 °C for 12 h in a vacuum furnace. Subsequent ageing treatments were performed at 900 °C in air for times of 200 h, 500 h, 1000 h, 2000 h, 5000 h and 10000 h. After ageing the specimens were air cooled. The solution and

ageing treatment temperature employed was based on the melting points and  $\gamma'$  solvus temperatures reported in [18].

### 2.3. Microstructure characterization

The specimens for microstructural characterization by scanning electron microscopy (SEM) were prepared by grinding, polishing, and then electro-polishing for 90 s in a solution of 2-buthanol and perchloric acid in methanol at  $-41\text{ }^{\circ}\text{C}$  with a voltage of 25 V. Backscattered Electron (BSE) images as well as Electron Backscattered Diffraction (EBSD) maps were obtained using a Leo Gemini 1530 and a Zeiss Auriga SEM both equipped with field emission electron guns and TSL EBSD analysis systems. The transmission electron microscope (TEM) specimens were cut and ground to about  $60\text{ }\mu\text{m}$  thickness and subsequently electrolytically thinned to electron transparency using the Struers A3 electrolyte with a voltage of 20 V at  $-38\text{ }^{\circ}\text{C}$ . They were investigated using a Philips CM200 TEM operated at 200 kV. X-ray diffraction (XRD) measurements were carried out to identify the phases in the specimens. Room temperature XRD was conducted using a Siemens D5000 diffractometer at 40 kV and 40 mA, the wavelength of the X-rays corresponded to copper  $K\alpha$  ( $1.5418\text{ \AA}$ ). Additional diffraction measurements were performed at the synchrotron radiation beamline HEMS run by Helmholtz-Zentrum Geesthacht at PETRA III of the Deutsches Elektronen-Synchrotron (DESY), Hamburg, Germany. The specimens had a 5 mm diameter and were measured in transmission with a beam size of  $1\text{ mm} \times 1\text{ mm}$  and an X-ray energy of 100 keV ( $\lambda = 0.1240\text{ \AA}$ ).

The area fraction of  $\text{D0}_{19}$  phase was determined from the SEM micrographs using the software ImageJ with the threshold-based segmentation method. The area of B2 phase was ignored because of its extremely small amount and its distribution around  $\text{D0}_{19}$  needles or at grain boundaries. The area fraction and particle size of the  $\gamma'$  precipitates were determined using the line segment intersection method in Photoshop. For every specimen at least 400 precipitates in 4 different areas within the  $\gamma/\gamma'$  regions with their surface parallel to  $\{001\}$  planes were included in the measurements. To determine the real fraction of  $\gamma'$  phase the measured area fraction was corrected by excluding the  $\text{D0}_{19}$  area fraction. As the  $\gamma'$  particles were cubic and distributed quite evenly, the area fraction directly determined from the micrographs was assumed to be equal to the volume fraction.

## 3. Results and discussion

### 3.1. Microstructural evolution

The microstructures of the 8W, 9W and 11W alloys after ageing at  $900\text{ }^{\circ}\text{C}$  for times between 200 h and 10000 h are shown in [Fig. 1](#). All micrographs were taken using the SEM backscattering mode. It is clearly visible that even after ageing for 10000 h the microstructure

predominantly consists of the  $\gamma$  (Co) matrix with homogeneously distributed cubic  $\gamma'$  ( $\text{Co}_3(\text{Al,W})$ ) particles as the primary precipitate phase in the matrix. Additional phases appearing brighter in the images are also present, which seem to increase in fraction and size in all three alloys with increasing ageing time.

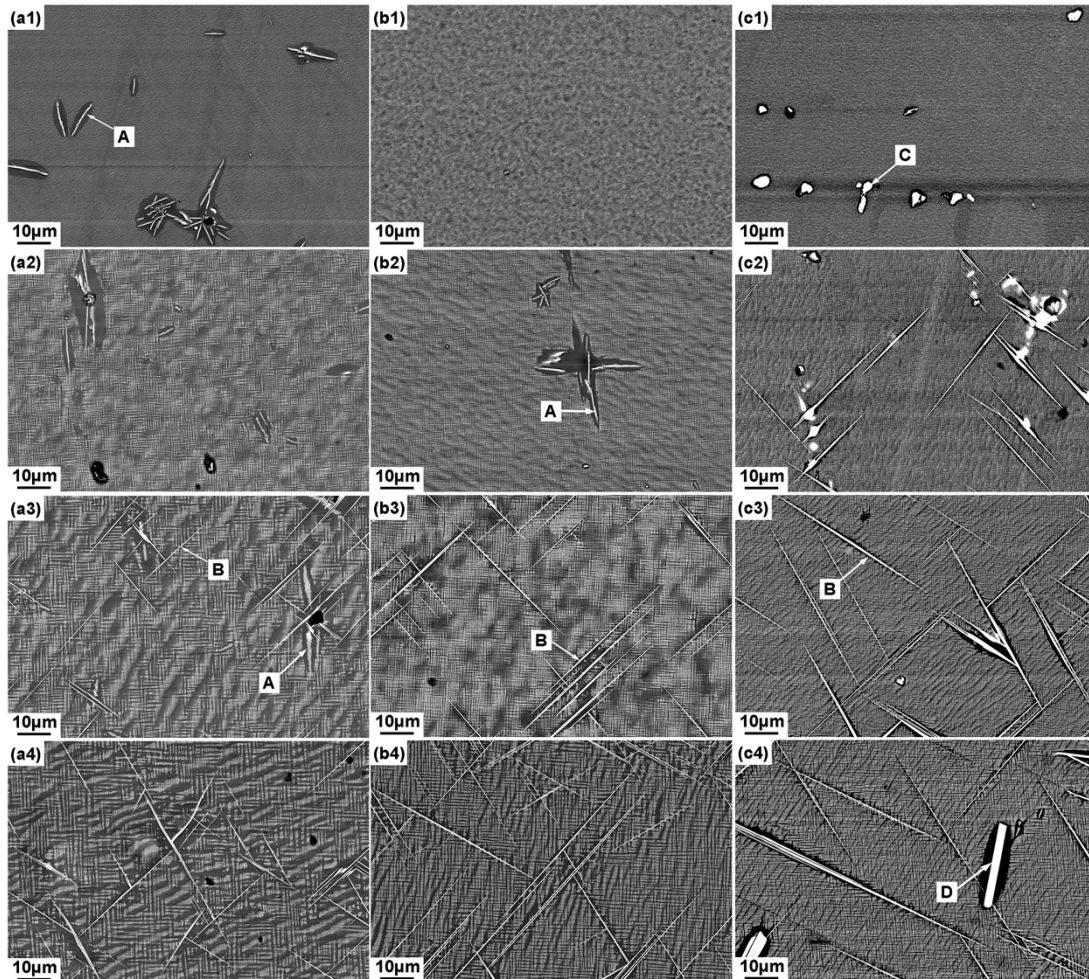


Fig. 1 BSE micrographs viewed from near the  $\langle 001 \rangle$  direction showing the microstructural evolution during long term ageing at 900 °C. a - 8W; b - 9W; c - 11W. 1 - 200 h; 2 - 2000 h; 3 - 5000 h; 4 - 10000 h. Labels A to D mark differently shaped  $\text{D0}_{19}$  particles and will be discussed later in conjunction with other results.

To identify the type of these additional phases, XRD and analysis of selected area diffraction pattern (SADP) in TEM were employed. Fig. 2a - c) show the XRD patterns of the three boron containing alloys after ageing for 200 h and 2000 h as well as the HEXRD pattern of the alloy Co-9Al-9W after ageing for 5000 h shown in Fig. 2d. The positions where diffraction peaks are expected for the phases  $\gamma'$ ,  $\text{D0}_{19}$  and B2 are indicated. The majority of the diffraction peaks from the  $\gamma$  phase overlap with those of  $\gamma'$  phase due to their similar crystal structure and lattice constants. Thus,  $\gamma$  phase peaks are not separately marked in Fig. 2. In addition to the desired  $\gamma/\gamma'$  phases, a  $\text{D0}_{19}$  phase is present in 8W and 9W already in a specimen state which can be considered as kind of standard heat-treated (200 h). Only one small  $\text{D0}_{19}$  peak is found in 11W after ageing for 200 h which probably corresponds to the

bright particles visible in [Fig. 1c1](#). The reason why only one weak peak of this phase is detected may be due to its very low volume fraction or an unsuitable orientation of the phase to satisfy the diffraction conditions. For all three alloys a number of somewhat stronger  $D0_{19}$  peaks are present in the diffractogram after ageing for 2000 h, indicating that the volume fraction of  $D0_{19}$  phase increases with ageing time. In addition, small peaks indicating the presence of some B2 phase are found after 2000 h. There are several additional small diffraction peaks not marked at about  $39^\circ$  and  $61^\circ$  in Fig. 2 (2000 h in a, b, c). These can be identified as CoO from a thin oxide layer which grew during the extended ageing of the 2000 h specimens. Based on the SEM and XRD investigations it can be concluded that the  $\gamma/\gamma'$  phases exist as the primary phases up to extended ageing times at a typical service temperature of  $900^\circ\text{C}$ . Nevertheless, additional  $D0_{19}$  phase is found to have formed after ageing for 200 h and its volume fraction increases after ageing for 2000 h. A very small amount of B2 phase was found in all three alloys after 2000 h ageing. The higher W content seems to delay the formation of the  $D0_{19}\text{-Co}_3\text{W}$  phase in the 11W alloy. These findings are in agreement with the results published by Lass et al. [14,21]. In the boron free Co-9Al-9W alloy, peaks corresponding to the phases  $\gamma$ ,  $\gamma'$  and  $D0_{19}$  are visible after ageing at  $900^\circ\text{C}$  for 5000 h. B2 is either absent or perhaps its primary (110) diffraction peak was overlapped by the (111) peaks of  $\gamma/\gamma'$  phase. Another possible reason is that the amount of B2 phase is below to the detection limit. From the results it can be concluded that the small addition of boron makes no principal difference with respect to phase stability at  $900^\circ\text{C}$ . In the boron free ternary alloy, in addition to the  $\gamma$  and  $\gamma'$  phases, the  $D0_{19}$  phase has also formed after extended ageing at  $900^\circ\text{C}$ .

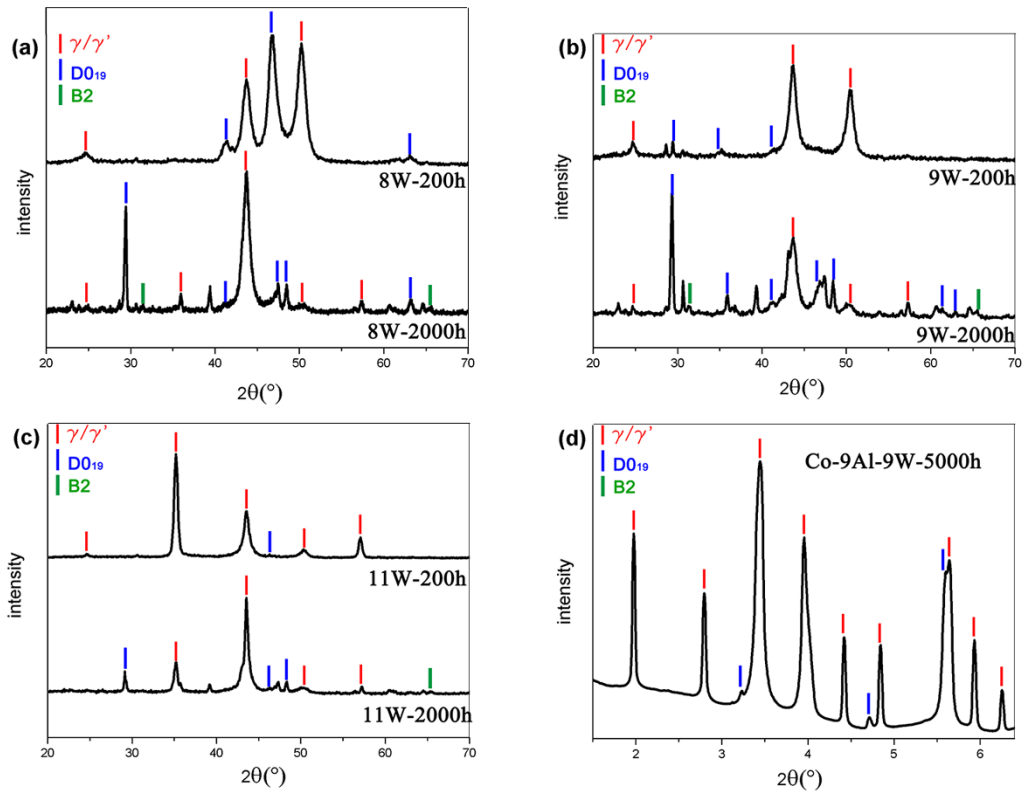


Fig. 2 XRD patterns of a. 8W, b. 9W, c. 11W with boron after 200 and 2000 h ageing at 900 °C showing the changing of the D0<sub>19</sub> and B2 phases during heat-treatments. d. Synchrotron HEXRD pattern of Co-9Al-9W without boron after 5000 h ageing at 900 °C.

The results of the XRD investigations have been supplemented by TEM characterization of aged 8W, 9W and 11W alloy specimens. The aim of this was to confirm the XRD results, associate the different phases to the different precipitates morphologies and to find any precipitate phase present with such a low volume fraction or small size that they were not detected by XRD. [Fig. 3](#) shows typical precipitates present in the 8W, 9W and 11W alloys after ageing for 10000 h together with the corresponding SADPs. Most of the precipitates exhibit a needle-shape, but with differing aspect ratios. However in the 11W alloy more bulky or plate-like particles were also observed using both SEM (see corner of [Fig. 3d](#)) and TEM (see [Fig. 3d](#)). It is assumed, at least in the 11W alloy, that a few plate-like shaped particles of D0<sub>19</sub> phase exist. From the SADPs all precipitates were identified as D0<sub>19</sub> phase. By analyzing SADPs of precipitates and the neighboring matrix for some of the D0<sub>19</sub> precipitates, an orientation relationship of  $\langle 110 \rangle_{\gamma} \parallel \langle 11-20 \rangle_{D0_{19}}$  and  $(111)_{\gamma} \parallel (0001)_{D0_{19}}$  was determined. It is interesting to note that while peaks indicating D0<sub>19</sub> and B2 phases were found in the XRD patterns after extended ageing, only D0<sub>19</sub> precipitates were identified by TEM investigation.

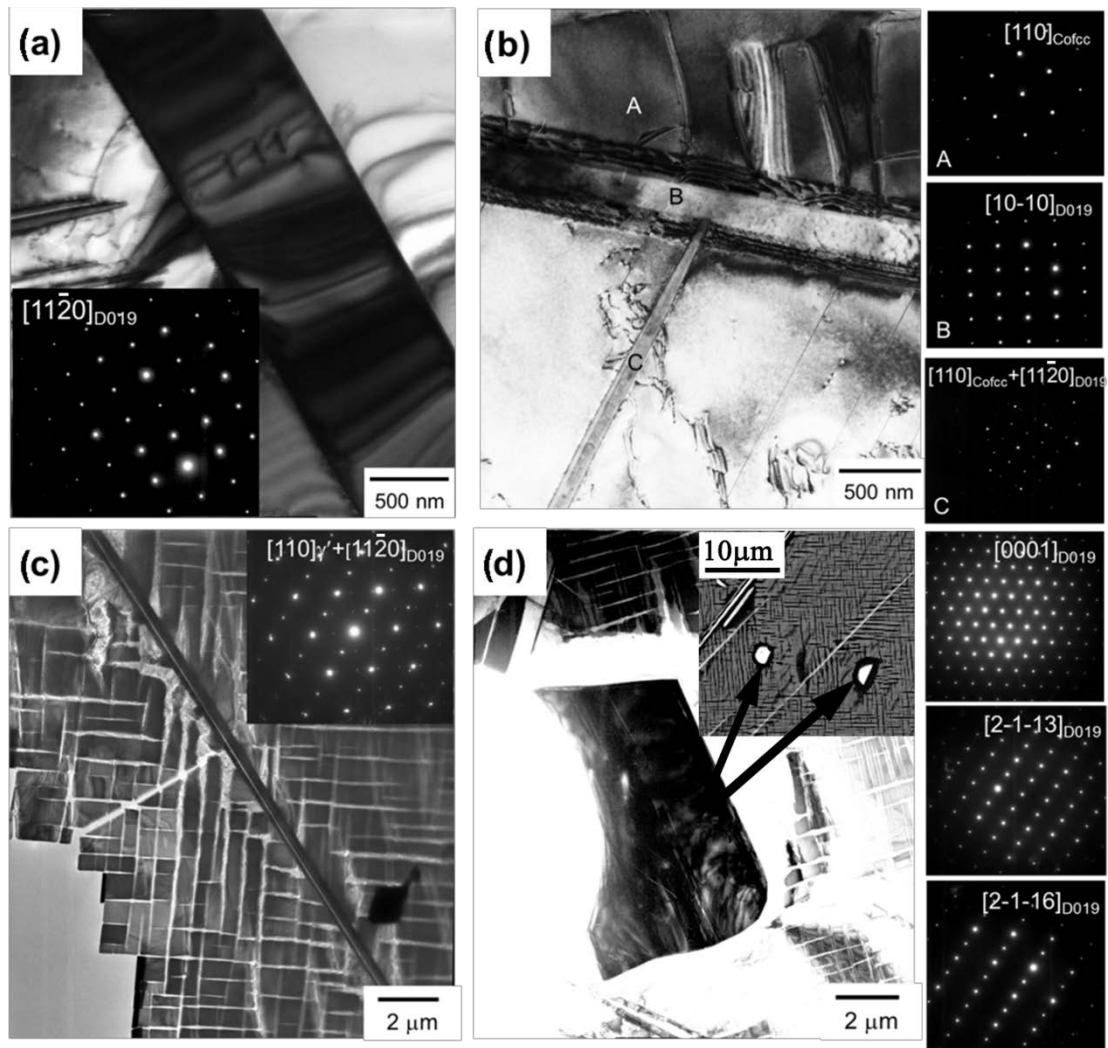


Fig. 3 Transmission electron micrographs and diffraction patterns of the 8W, 9W and 11W alloys after ageing for 10000 h at 900 °C. a - D0<sub>19</sub> phase and corresponding SADP in 8W; b - two D0<sub>19</sub> phase precipitates in 9W with SADP of the neighboring matrix (A), of the bigger D0<sub>19</sub> precipitate (B) and the combined pattern of the smaller D0<sub>19</sub> precipitate and the matrix (C); c - needle-like D0<sub>19</sub> precipitate in the 11W alloy with combined SADP of the matrix and the D0<sub>19</sub> precipitate; d - bulky D0<sub>19</sub> particle in the 11W alloy with SADPs of the particle from three different beam directions and a SEM image of the same ageing condition in the upper right corner (particles marked by arrows).

Contrary to the XRD results, TEM did not positively identify the presence of B2 phase after ageing for up to 10000 h. Thus EBSD in the SEM was used as a third method to identify the phases present in the three alloys after ageing. In Fig. 4 phase maps of grain boundary regions in the 8W, 9W and 11W alloys are shown for specimens aged for 10000 h at 900 °C. The major part of the microstructure consists of the  $\gamma/\gamma'$  phases shown in light green. Due to their close crystallographic similarity it was not possible to differentiate between the  $\gamma$  matrix and  $\gamma'$  precipitates by EBSD. Most of the other precipitates exhibit a D0<sub>19</sub> crystal structure and are shown in dark green. They have either a needle-like shape or exhibit a more blocky appearance especially at the grain boundaries of 8W and in 11W. Except for one larger region in 9W, it is clear that B2 particles (shown in red) are located at, or close to the grain

boundaries, and are merged with some  $D0_{19}$  particles, thus explaining the difficulties in finding this phase in TEM. The cooperative growth of B2 around  $D0_{19}$  could accelerate the overall transformation because Al rejected from the  $D0_{19}$  phase when transforming out of  $\gamma'$  phase can be directly consumed by the forming B2 phase making long range diffusion unnecessary.

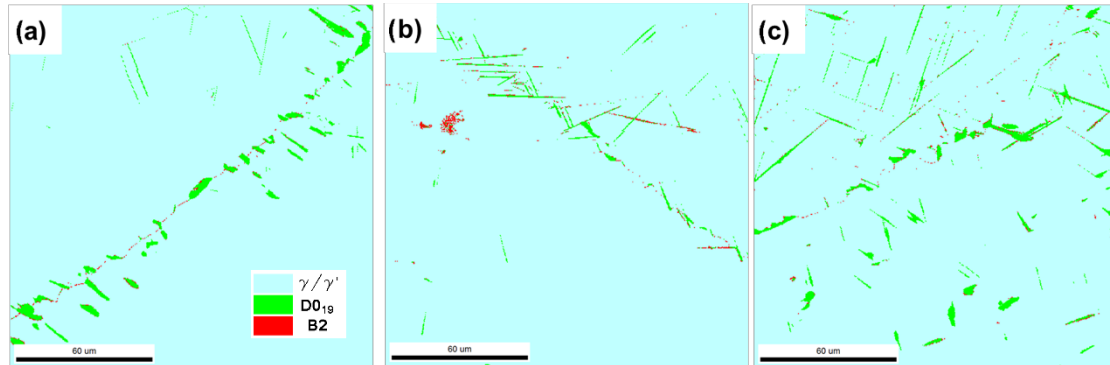


Fig. 4 EBSD phase maps of the 8W, 9W and 11W alloys after 10000 h aging at 900 °C; the  $\gamma/\gamma'$  phase is shown in light green,  $D0_{19}$  phase in dark green and the B2 phase in red. A - 8W; b - 9W; c - 11W.

As shown in [Fig. 1](#), a small amount of  $D0_{19}$  phase is clearly visible as small needles, marked as A in 8W ([Fig. 1a1, a2](#)) and 9W ([Fig. 1b2](#)). After further ageing up to 5000 h, the  $D0_{19}$  needles became much longer and thinner in 8W ([Fig. 1a3, a4](#)) and 9W ([Fig. 1b3, b4](#)) (marked as B). This is in agreement with the morphology of  $D0_{19}$  phase that was reported in the literature [22] and found during the TEM investigations described above. In the 11W alloy, the  $D0_{19}$  phase exhibits a different morphology of small white plates that are marked (C) in [Fig. 1c1](#), compared to that in 8W and 9W before 500 h ageing. The precipitates subsequently grew longer, in a similar way to those observed in 8W and 9W, after 2000 h ageing. In addition, a small fraction of the  $D0_{19}$  needles transformed into thicker rods (marked as D) in [Fig. 4c4](#) when the ageing time was increased to 10000 h.

### 3.2. $\gamma/\gamma'$ microstructure

Details of the  $\gamma/\gamma'$  two-phase microstructure after different ageing times are shown on the micrographs in [Fig. 5](#). The images were obtained, using SEM in the backscattered electron mode, from near  $\{001\}$  sections of the 8W ([Fig. 5a1 - a6](#)), 9W ([Fig. 5b1 - b6](#)), and 11W ([Fig. 5c1 - c6](#)) alloys. All three alloys consist of cubic  $\gamma'$  precipitates embedded in the  $\gamma$  matrix. Comparing the microstructures shown in [Fig. 5](#) at similar ageing times, the  $\gamma'$  precipitates within the 11W alloy are arranged most densely with only narrow  $\gamma$  matrix channels separating them. In the 9W alloy the matrix channels are significantly wider, while the least dense arrangement of  $\gamma'$  precipitates with the broadest matrix channels was found in 8W. Thus, with increasing W content and the corresponding increase of the  $\gamma'$  volume fraction, the  $\gamma$  matrix channels become narrower and the  $\gamma'$  precipitates better aligned. In the 11W alloy the  $\gamma'$  precipitates start to grow together along the  $\langle 001 \rangle$  directions, while in the 8W alloy they

are arranged more randomly and are less well aligned. This is especially true for ageing times shorter than 200 h which were also investigated, but which are not presented in this paper. The shape of the  $\gamma'$  precipitates in the 11W alloy more or less resemble perfect cubes with sharper edges and corners compared to  $\gamma'$  precipitates in the 8W and 9W alloys which appear to be more rounded. During the ageing process, the  $\gamma'$  precipitates in all three alloys rapidly coarsen and align along the different  $\langle 001 \rangle$  directions, and the channels between precipitates become wider, most obviously seen in 8W. In [Fig. 5](#) it can be seen that some smaller particles visible in the early stages of ageing (marked as C), tend to merge with larger adjacent ones, resulting in a rapid discontinuous coarsening of these bigger particles.

The  $\gamma'$  precipitates in the 8W alloy become less rounded after extended ageing, and some oblong shaped particles were present after 2000/5000 h, marked (A) in [Fig. 5a4 - a5](#). Nevertheless, the  $\gamma'$  precipitates around these oblong shaped particles seemed to increase in diameter and remained cubic instead of elongating. After 10000 h more oblong shaped particles had formed and some of the cube corners had seemingly dissolved or re-orientated, leaving irregularly shaped particles as marked (B) in [Fig. 5a6](#). In general, the development of the  $\gamma'$  precipitate morphology in the 9W alloy is similar to that in the 8W alloy, but the shape appears to be more stable, consisting mostly of regular cubes already after 200 h of ageing. The occurrence of oblong shaped particles in 9W, marked (A) in [Fig. 5b5 - b6](#), took place after 5000 h, which is later than in 8W, and arise more seldom. In contrast, many  $\gamma'$  precipitates in the 11W alloy have a T- or L-shape morphology, marked (C) in [Fig. 5c1 - c4](#), because precipitates that were aligned along different  $\langle 001 \rangle$  directions have grown together during the earlier stages of ageing, before forming larger cubes after extended ageing to 5000 h. It is tempting to speculate if the appearance of oblong shaped particles is connected with the dissolution of the  $\gamma'$  phase. Indeed it will be shown later ([Fig. 8a](#)) that 8W shows the strongest decrease in  $\gamma'$  volume fraction after extended ageing and also most frequently exhibits such oblong shaped particles.

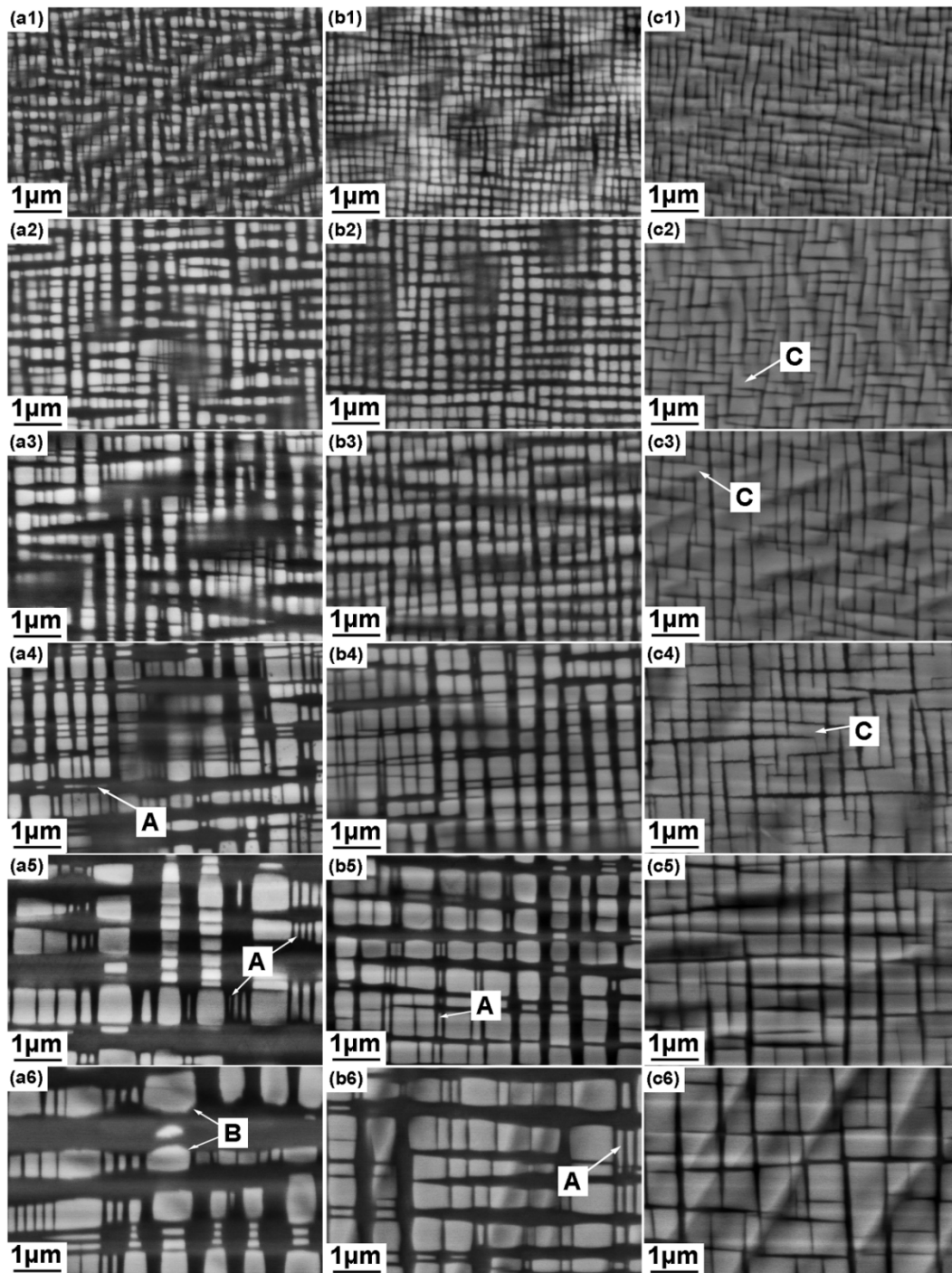


Fig. 5 BSE micrographs viewed closely along the  $\langle 001 \rangle$  orientation showing the evolution of the  $\gamma/\gamma'$  two-phase microstructure during long-term ageing at 900 °C. a - 8W; b - 9W; c - 11W. 1 - 200 h; 2 - 500 h; 3 - 1000 h; 4 - 2000 h; 5 - 5000 h; 6 - 10000 h.

The  $\gamma/\gamma'$  microstructures of the 8W, 9W and 11W alloys are imaged in more detail using TEM in Fig. 6a - c. All micrographs were taken in the bright field multi-beam condition with a viewing direction near the  $\langle 001 \rangle$  orientations. According to the SADPs of the  $\langle 001 \rangle$  directions, all  $\gamma'$  precipitates still show the initial orientation relationship with the matrix of  $(001)_{\gamma'} \parallel (001)_{\gamma}$  and  $[100]_{\gamma'} \parallel [100]_{\gamma}$  even after 10000 h of ageing.

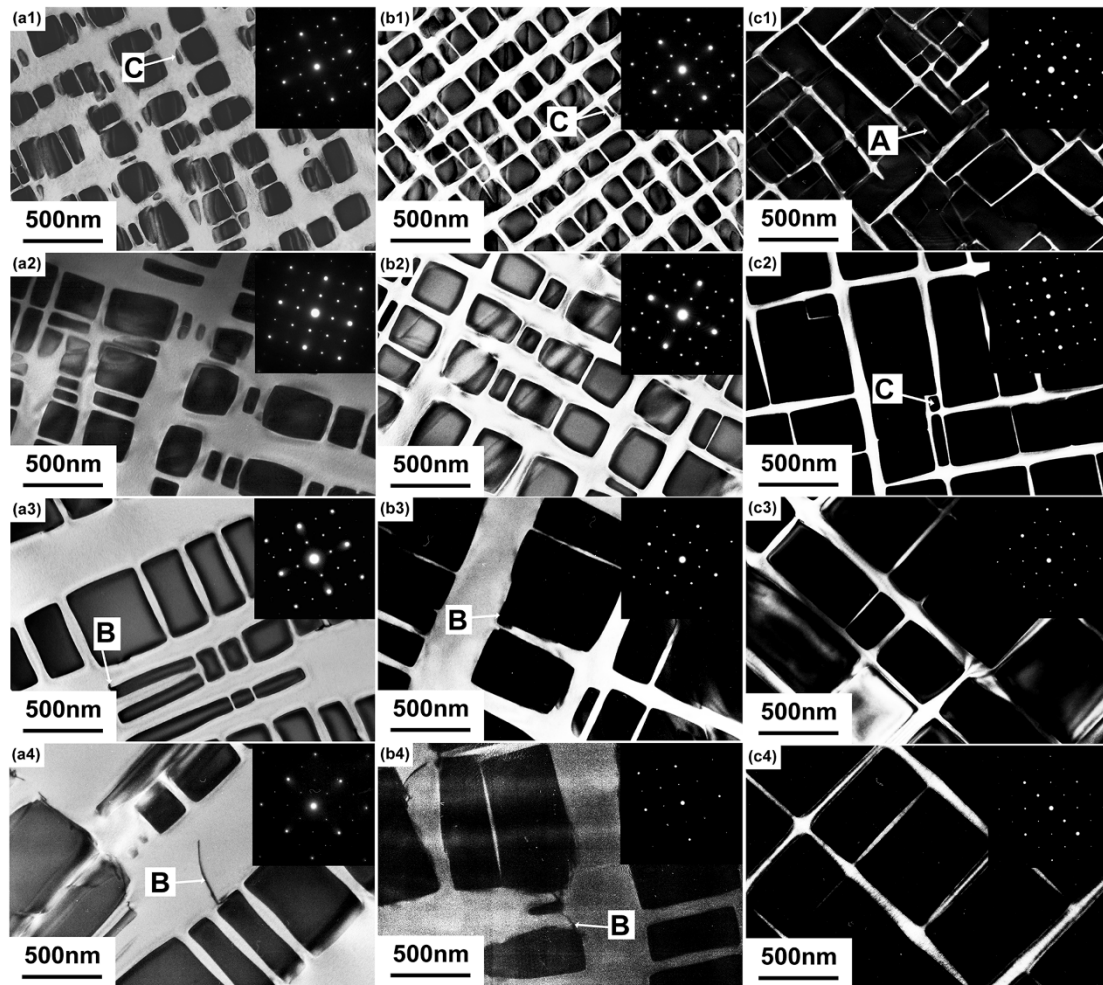


Fig. 6 TEM bright field images and corresponding SADPs showing the evolution of the  $\gamma/\gamma'$  two-phase microstructure during long-term ageing at 900 °C. a - 8W; b - 9W; c - 11W. 1 - 200 h; 2 - 1000 h; 3 - 5000 h; 4 - 10000 h.

It is clearly recognizable, especially in 11W, that some narrow matrix channels exist between adjacent  $\gamma'$  precipitates that are barely visible and that the precipitates almost connect with each other during the early period of ageing, marked (A) in Fig. 6c1. The densely packed  $\gamma'$  particles at (A) gradually grow together to form large precipitates as ageing proceeds. Moreover, during further ageing up to 5000 h, the remaining tiny  $\gamma'$  precipitates at (C) seem to merge with neighbouring particles to form bigger particles. Furthermore, some dislocation segments are observed around the  $\gamma'$  precipitates in the 8W and 9W alloys after longer ageing times, marked (B) in Fig. 6a3 - a4, b3 - b4. This is even more clearly visible in Fig. 10 which is shown later. The presence of dislocations may support the dissolution or re-orientation of the precipitate corners, as already shown in Fig. 5a6, because the dislocations may act as diffusion channels accelerating morphology changes in their vicinity. Another possible reason for the re-orientation of the precipitate corners could be a partial loss of coherency at the  $\gamma/\gamma'$  interfaces due to interfacial dislocations making interfaces parallel to  $\{001\}$  planes less favourable.

The  $\gamma'$  precipitate size (see [Fig. 7](#)) as well as the volume fraction (see [Fig. 8a](#)) increase with increasing W content. The size is represented by the average equivalent diameter of the  $\gamma'$  precipitates' side. In addition to the size of the  $\gamma'$  precipitates increasing with W content, it can also be seen that the  $\gamma'$  precipitates coarsen during long-term ageing but with different rates depending on alloy composition. If the driving force for the coarsening process is the reduction of total interfacial energy, then the development of precipitate size with time, for precipitates dispersed in a matrix, should obey the Lifshitz, Slyozov and Wagner (LSW) theory [23-25]. This theory predicts precipitate coarsening according to the relationship,  $D^3 = kt$ , when the coarsening rate is diffusion-controlled. Here  $D$  (nm) is the average diameter of the precipitate,  $t$  (h) is the ageing time and  $k$  is the coarsening rate constant. The modified equation,  $D^n = kt$ , was used to fit the measured  $\gamma'$  precipitates size against ageing time. The results are shown below for the different alloys:

$$(D_{8W})^{3.048} = 2.187 \times 10^4 \times t$$

$$(D_{9W})^{3.125} = 4.482 \times 10^4 \times t$$

$$(D_{11W})^{3.676} = 5.621 \times 10^6 \times t$$

The values of  $n$  are 3.048 for the 8W alloy, 3.125 for 9W and 3.676 for the 11W alloy. These values indicate that the coarsening of precipitates in the 8W alloy most closely matches the behavior expected in accordance with the LSW theory. That the values of  $n$  for all three alloys slightly deviate from 3, expected from the LSW theory, is probably due to the fact that the LSW theory describes coarsening for a dilute solution while the current alloys contain rather densely packed precipitates. This is supported by the fact that the strongest deviation of  $n$  occurs in the 11W alloy which has the highest  $\gamma'$  volume fraction and most densely packed precipitates. Here it is also mentioned that due to different lattice mismatch different coherency stresses may occur in the alloys which in general were not taken into account in the LSW theory [25]. The value of  $k$  increases from  $2.187 \times 10^4$  for the 8W alloy to  $4.482 \times 10^4$  for 9W to  $5.621 \times 10^6$  for 11W. Thus, the coarsening rate increases with the volume fraction of  $\gamma'$  phase and thus with the W content of the alloy (see [Fig. 8a](#)) in agreement with the literature [14,26]. Additionally, a uniform size of the  $\gamma'$  precipitates can decrease the coarsening rate. The error bars in [Fig. 7](#) stand for the standard deviation. The wider distribution of precipitate sizes in 11W may also contribute for the fastest coarsening rate in this alloy [26]. It is interesting to note that these effects that can accelerate coarsening in 11W seem to counteract a slower diffusion rate in this alloy which could be expected from the higher W content. This seems to be compensated by the higher  $\gamma'$  volume fraction of 11W which is reported in literature to accelerate coarsening [27].

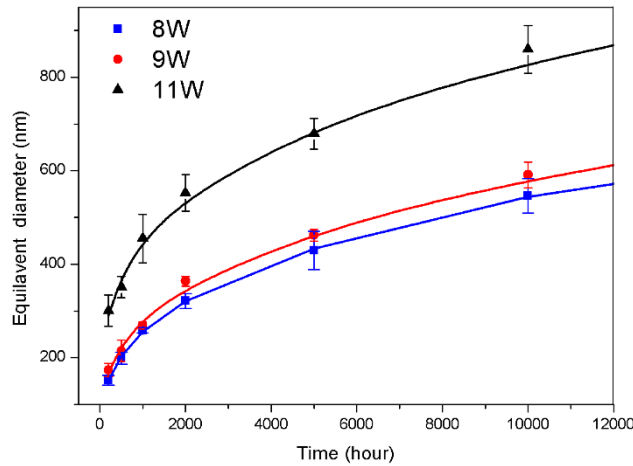


Fig. 7 equivalent diameter of  $\gamma'$  precipitates plotted against ageing time – the lines represent a  $D^n = kt$  fit of the data according to LSW (Lifshitz, Slyozov and Wagner) theory.

In general, the volume fraction of the  $\gamma'$  phase increases with increasing W content but decreases during ageing in all three alloys (see Fig. 8a). The area fraction of the bright additional phases, which are probably predominantly  $D0_{19}$ , is plotted in Fig. 8b and increases continually with ageing time in all three alloys. The measurement data is not accurate enough to decide whether in 11W after about 2000 hours still a slight increase or a saturation is observed. A small initial increase in the volume fraction of  $\gamma'$  precipitates is observed in the 11W alloy prior to 500 h ageing as shown in Fig. 8.a. This is probably caused by the high amount of W in this alloy slowing down diffusion that delayed the complete nucleation of  $\gamma'$  precipitates. Based on Fig. 1 and literature data [13,15], it can be concluded that at least some of the  $\gamma'$  phase decomposes into  $D0_{19}$  phase during long time ageing. This is supported by the decrease of  $\gamma'$  volume fraction observed, at least in the 8W and 9W alloys, after extended ageing times.

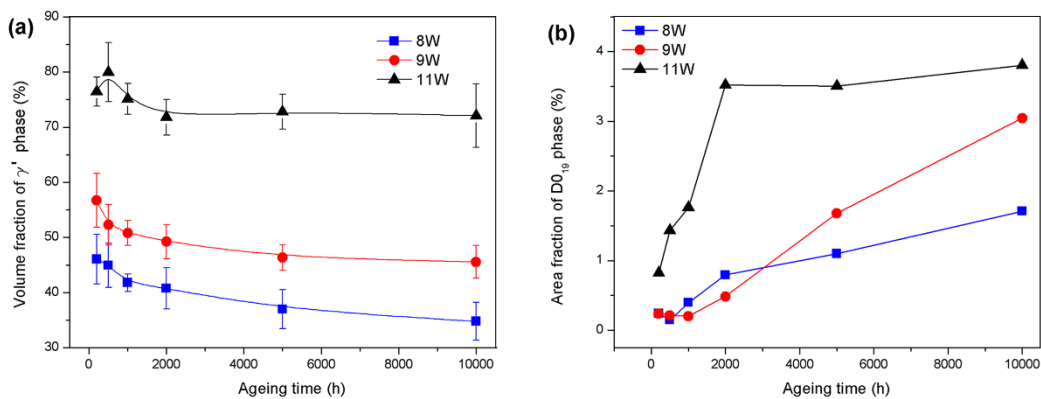


Fig. 8 Variation of a) volume fraction of  $\gamma'$  precipitate and b) area fraction of  $D0_{19}$  phase with ageing time.

From Fig. 8, it can be seen that the decomposition of the  $\gamma'$  phase during ageing is most rapid in the 8W and 9W alloys. In other words, the most stable  $\gamma'$  phase with respect to its

retained fraction exists in the 11W alloy. Nevertheless, quite large volume fractions of  $\gamma'$  phase still exist in all three alloys even after ageing for 10000 h. However, the decreasing  $\gamma'$  volume fraction and the formation of  $DO_{19}$  phase during ageing indicates that the stable phase constitution at 900 °C for all three alloys is either within a three phase ( $\gamma - \gamma' - DO_{19}$ ) region or, if the  $\gamma'$  phase is metastable, a three phase ( $\gamma - B2 - DO_{19}$ ) region.

TEM micrographs recorded using a two-beam dark field condition with the (100) superlattice diffraction and the specimen orientated near the  $\langle 001 \rangle$  direction are shown in Fig. 9. Secondary  $\gamma'$  precipitates exist in all three alloys during the earlier stages of ageing. The tiny secondary  $\gamma'$  precipitates are clearly visible in the broad matrix channels of the 8W and 9W alloys, while fewer and finer particles have precipitated in the narrower channels within the 11W alloy. No secondary  $\gamma'$  precipitates were observed after extended ageing times longer than 200 h.

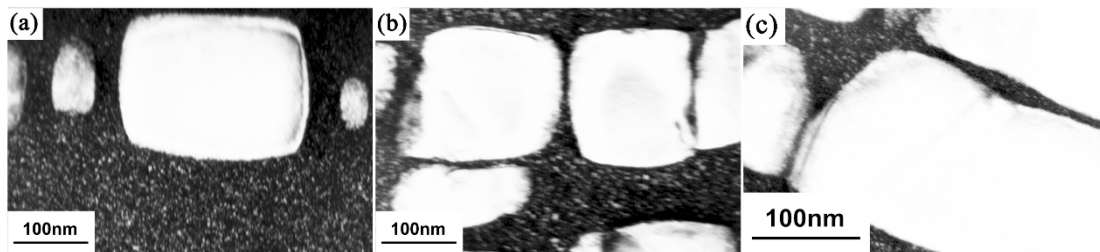


Fig. 9 TEM dark field images of the  $\gamma/\gamma'$  two-phase microstructure and secondary  $\gamma'$  precipitates observed during the early stage of ageing, after 200 h at 900 °C. a - 8W; b - 9W; c - 11W. Images were taken along the [001] direction with the  $g = 100\gamma$  superlattice reflection.

### 3.3. $L1_2$ to $DO_{19}$ phase transformation

It is inferred from Fig. 1 and Fig. 8 that at least some of the cubic  $L1_2-\gamma'$  precipitates decompose into the hexagonal  $DO_{19}-Co_3W$  phase during ageing. TEM images in Fig. 10 show the microstructure of the three alloys after extended periods of ageing. In Fig. 10a some dislocations and stacking faults are located among the  $L1_2-\gamma'$  precipitates, which are probably the first step in the decomposition of the  $L1_2-\gamma'$  phase into the  $DO_{19}$  phase. When imaged along the [001] direction of the  $L1_2$  lattice, the stacking faults and  $DO_{19}$  needles are parallel to [110] directions, as shown in Fig. 10b - d. Moreover, there are always some stacking faults adjacent to  $DO_{19}$  needles (marked by rectangles in Fig. 10b - d), which indicates that the stacking faults seem to be connected with the  $L1_2-\gamma'$  to  $DO_{19}$  phase transformation. The crystal structures and the orientation relationship between the  $L1_2$  and  $DO_{19}$  phases are illustrated in Fig. 11. The  $L1_2$  and  $DO_{19}$  phases exhibit the following OR:  $(111)_{L1_2} \parallel (0001)_{DO_{19}}$ ,  $\langle 112 \rangle_{L1_2} \parallel \langle 1-100 \rangle_{DO_{19}}$  [22].

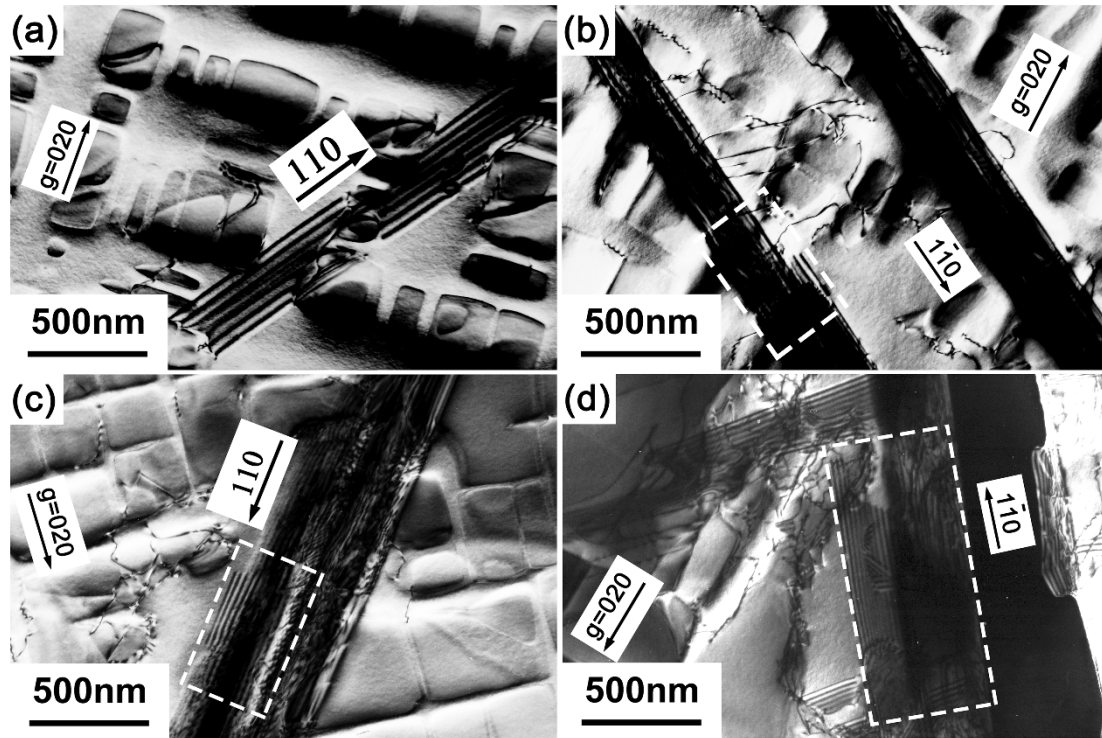


Fig. 10 TEM two-beam dark field images of the three alloys after long-term ageing at 900 °C. a - 8W, 1000 h: stacking faults along a  $[110]$  direction among  $\gamma'$  cubes; b - 9W, 1000 h: stacking faults adjacent to  $D0_{19}$  needles; c - 11W, 1000 h and d - 11W, 5000 h: stacking faults adjacent to  $D0_{19}$  needles. Images were taken with  $B = 001$ ,  $g = 020$ .

Based on the observations reported above, a stacking fault based transformation mechanism from the  $L1_2$ - $\gamma'$  to the  $D0_{19}$  phase can be assumed, which has also been reported for other systems [22,28] and is schematically shown in Fig. 12. The  $L1_2$ - $\gamma'$  phase possesses an arrangement of atoms that is akin to a fcc lattice, despite its ordered structure, with a sequence of atomic  $\{111\}$  layers of ABCABCABC. To transform into the hexagonal  $D0_{19}$  phase with an ABABAB layer arrangement of  $(0001)$  planes which are parallel to the  $\{111\}$  planes of the  $L1_2$  phase, a stacking fault based mechanism could operate. The atoms in layer C move along the  $\langle 112 \rangle$  direction by a distance of  $a/3$  to occupy atomic positions of layer A in the  $\{111\}$  plane. This results in a stacking fault that changes the ordering to ABCAB $\downarrow$ ABC. Thus a C layer is removed. But also the atomic ordering in the two neighbouring lattice planes is changed to that of the  $D0_{19}$  phase. If such a mechanism operated on every second layer, then the atomic arrangement would be changed to that of the  $D0_{19}$  phase. According to [22,28] this process does often not take place in a single step. Firstly the atoms in the C layer move along the  $[2-1-1]$  direction by  $a/6$  to form a lattice where the atoms assume the positions of hcp structure, and then slide further by  $a/6[11-2]$  and  $a/6[12-1]$  to obtain the final  $D0_{19}$  structure where also the correct species of atoms sits on its respective lattice positions. That is to say, that by operation of  $a/6[112]\{111\}$  partials which combine to a  $a/3[11-2]\{111\}$  superpartial, the correct atomic arrangement and ordering of the  $D0_{19}$  phase are achieved.

When we transfer this concept to the transformation of  $L1_2\text{-Co}_3(\text{Al,W})$  to  $D0_{19}\text{-Co}_3\text{W}$  it is necessary to consider that also the chemical composition of the involved phases differ. Thus, the mechanism described above which is based on shifts of atoms has to be accompanied by long range diffusion of Al away from the  $D0_{19}$  phase and of W to the  $D0_{19}$  phase.

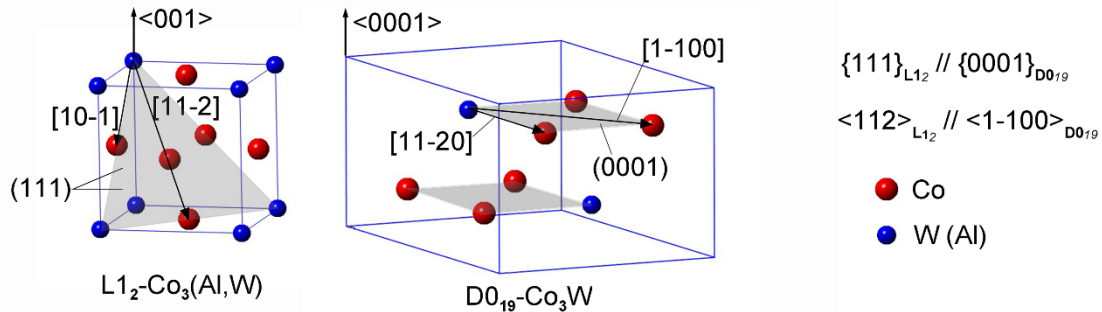


Fig. 11 Crystal structure of  $L1_2$  and  $D0_{19}$  phases. The directions and planes to define the orientation relationship between the two phases are marked.

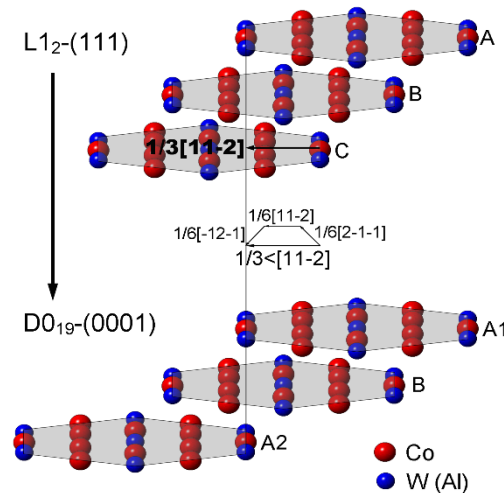


Fig. 12 Atomic layer movement in the  $L1_2$  to  $D0_{19}$  transformation: atoms in layer C of  $L1_2$  move to positions of layer A2 in  $D0_{19}$  along  $1/6\langle 112 \rangle$  by three steps.

#### 4. Conclusions

- In  $\text{Co-9Al-(8,9,11)W-0.1B}$  alloys, a microstructure consisting of the  $\gamma$  matrix,  $\gamma'$ - $L1_2$  phase,  $D0_{19}$  phase and B2 phase is found after extended ageing up to 10000 h at 900 °C.
- In all three alloys investigated, the  $\gamma'$  phase decomposes into the  $D0_{19}$  phase during the ageing process at 900 °C. Nevertheless, a significant fraction (34.8%, 48.0%, 74.9% for the 8W, 9W, 11W alloys respectively) of  $\gamma'$  phase still remains after 10000 h ageing at 900 °C.

- During ageing at 900 °C the  $\gamma'$  precipitates coarsen with increasing ageing time roughly in accordance with the modified LSW theory ( $D^n = kt$ ). Coarsening of the  $\gamma'$  precipitates can be described by:

$$(D_{8W})^{3.048} = 2.187 \times 10^4 \times t$$

$$(D_{9W})^{3.125} = 4.482 \times 10^4 \times t$$

$$(D_{11W})^{3.676} = 5.621 \times 10^6 \times t$$

where  $D$  (nm) is the precipitate diameter and  $t$  (h) the ageing time. Coarsening accelerates with increasing W content probably as an effect of the higher  $\gamma'$  volume fraction which increases in parallel with the W content.

- The volume fraction of  $\gamma'$  phase decreases during extended ageing, especially in the 8W and 9W alloys, due to the transformation of  $\gamma'$  phase into the D0<sub>19</sub> phase. In the 11W alloy this decrease in  $\gamma'$  volume fraction starts slightly delayed as not all  $\gamma'$  precipitates have nucleated at the beginning of the ageing process. Also, the  $\gamma'$  volume fraction remains almost constant in 11W after 2000 h ageing.
- The transformation process from the  $\gamma'$  phase into the D0<sub>19</sub> phase is associated with stacking faults. The transformation of the L1<sub>2</sub>- $\gamma'$  atomic structure to that of the D0<sub>19</sub> phase can be facilitated by the movement of suitable partial dislocations which probably generate the necessary stacking faults as an intermediate step of this transformation.

### Acknowledgement

The authors are grateful to Dr. Andreas Stark and Dirk Matthiessen for their assistance in conducting the experiments. Yuzhi Li acknowledges the funding from the China Scholarship Council program.

### References

- [1] J Sato, T Omori, K Oikawa, et al. Cobalt-base high-temperature alloys. *Science*. 312 (2006) 90-91.
- [2] C H T Sims, N S Stoloff, W C Hagel. *Superalloys II*. 1987.
- [3] A Suzuki, T M Pollock. High-temperature strength and deformation of  $\gamma/\gamma'$  two-phase Co-Al-W-base alloys. *Acta Materialia*. 56 (2008) 1288-1297.
- [4] A Bauer, S Neumeier, F Pyczak, and M Göken. Microstructure and creep strength of different  $\gamma/\gamma'$ -strengthened Co-base superalloy variants. *Scripta Materialia*. 63 (2010) 1197-1200.

- [5] A Bauer, S Neumeier, F Pyczak, R F Singer and M Göken. Creep properties of different  $\gamma'$ -strengthened Co-base superalloys. *Materials Science and Engineering: A*. 550 (2012) 333-341.
- [6] A Bauer, S Neumeier, F Pyczak, and M Göken. Creep Strength and Microstructure of Polycrystalline  $\gamma'$ -Strengthened Cobalt-Base Superalloys. in *Superalloys 2012*, edited by E.S. Huron, R.C. Reed, M.C. Hardy, M.J. Mills, R.E. Montero, P.D. Portella, and J. Telesman (The Minerals, Metals & Materials Society, Warrendale, PA. 2012 (2012) 695-703.
- [7] F Pyczak, A Bauer, M Göken, S Neumeier, U Lorenz, M Oehring, N Schell, A Schreyer, A Stark, F Symanzik. Plastic deformation mechanisms in a crept  $L_{12}$  hardened Co-base superalloy. *Materials Science & Engineering A*. 571 (2013) 13-18.
- [8] K Shinagawa, T Omori, J Sato, et al. Phase Equilibria and Microstructure on  $\gamma'$  phase in Co-Ni-Al-W System. *Materials transactions*. 49 (2008) 1474-1479.
- [9] T Omori, K Oikawa, J Sato, et al. Partition behavior of alloying elements and phase transformation temperatures in Co-Al-W-base quaternary systems. *Intermetallics*. 32 (2013) 274-283.
- [10] Q Yao, H Xing, J Sun. Structural stability and elastic property of the  $L_{12}$  ordered  $Co_3(Al, W)$  precipitate. *Applied physics letters*. 89 (2006) 1906.
- [11] K Tanaka, T Ohashi, K Kishida, et al. Single-crystal elastic constants of  $Co_3(Al, W)$  with the  $L_{12}$  structure. *Applied Physics Letters*. 91 (2007).
- [12] S Miura, K Ohkubo, T Mohri. Mechanical properties of Co-based  $L_{12}$  intermetallic compound  $Co_3(Al, W)$ . *Materials transactions*. 48 (2007) 2403-2408.
- [13] S Kobayashi, Y Tsukamoto, T Takasugi, et al. Determination of phase equilibria in the Co-rich Co-Al-W ternary system with a diffusion-couple technique. *Intermetallics*. 17 (2009) 1085-1089.
- [14] E A Lass, M E Williams, C E Campbell, et al.  $\gamma'$  phase stability and phase equilibrium in ternary Co-Al-W at 900 °C. *Journal of Phase Equilibria and Diffusion*. 35 (2014) 711-723.
- [15] Y Tsukamoto, S Kobayashi, T Takasugi. The Stability of  $\gamma'$ - $Co_3(Al, W)$  phase in Co-Al-W Ternary System. *Materials Science Forum*. Trans Tech Publications. 654 (2010) 448-451.
- [16] C Jiang. First-principles study of  $Co_3(Al, W)$  alloys using special quasi-random structures. *Scripta Materialia*. 59 (2008) 1075-1078.
- [17] J E Saal, C Wolverton. Thermodynamic stability of Co-Al-W  $L_{12}$   $\gamma'$ . *Acta Materialia*. 61 (2013) 2330-2338.
- [18] F Pyczak, A Bauer, M Göken, et al. The effect of tungsten content on the properties of  $L_{12}$ -hardened Co-Al-W alloys. *Journal of Alloys and Compounds*. 632 (2015) 110-115.

- [19] S Neumeier, L P Freund, M Göken. Novel wrought  $\gamma/\gamma'$  cobalt base superalloys with high strength and improved oxidation resistance. *Scripta Materialia*. 109 (2015) 104-107.
- [20] K Shinagawa, T Omori, K Oikawa, et al. Ductility enhancement by boron addition in Co-Al-W high-temperature alloys. *Scripta Materialia*. 61 (2009) 612-615.
- [21] E A Lass, R D Grist, M E Williams. Phase Equilibria and Microstructural Evolution in Ternary Co-Al-W Between 750 and 1100° C. *Journal of Phase Equilibria and Diffusion*. 37 (2016) 387-401.
- [22] P Carvalho, B J Kooi, J T M De Hosson. Identification of planar defects in  $D0_{19}$  phases using high-resolution transmission electron microscopy. *Philosophical magazine letters*. 81 (2001) 697-707.
- [23] P W Voorhees. The theory of Ostwald ripening. *Journal of Statistical Physics*. 38 (1985) 231-252.
- [24] C Wagner. Theorie der Alterung von Niederschlägen durch Umlösen (Ostwald-Reifung). *Z. Elektrochem.* 65 (1961) 895-898.
- [25] I M Lifshitz, V V Slyozov. The kinetics of precipitation of supersaturated solid solutions. *Journal of physics and chemistry of solids*. 19 (1961) 35-50.
- [26] A J Ardell. Isotropic fiber coarsening in unidirectionally solidified eutectic alloys. *Metallurgical Transactions*. 3 (1972) 1395-1401.
- [27] A Baldan. Review progress in Ostwald ripening theories and their applications to nickel-base superalloys Part I: Ostwald ripening theories. *Journal of materials science*. 37 (2002) 2171-2202.
- [28] P A Carvalho, P M Bronsveld, B J Kooi, et al. On the fcc $\rightarrow$  $D0_{19}$  transformation in Co-W alloys. *Acta Materialia*. 50 (2002) 4511-4526.